Karlsruhe Institute of Technology

FAKULTÄT FÜR PHYSIK
Institute for Beam Physics and Technology (IBPT)

Study of Noise in the Simulation of Collective Effects of Relativistic Electron Bunches

Bachelor Thesis
of

Johannes Leonhard Schestag

at the Institute for Beam Physics and Technology (IBPT)

Reviewer: Prof. Dr. Anke-Susanne Müller
Advisor: Dr. Minjie Yan

Bearbeitungszeit: 01.08.2017 – 07.03.2018

Erklärung zur Selbstständigkeit

Ich versichere, dass ich diese Arbeit selbstständig verfasst habe und keine anderen als die angegebenen Quellen und Hilfsmittel benutzt habe, die wörtlich oder inhaltlich übernommenen Stellen als solche kenntlich gemacht und die Satzung des KIT zur Sicherung guter wissenschaftlicher Praxis in der gültigen Fassung vom 27.11.2014 beachtet habe.

Karlsruhe, den 07.03.2018, _____

Johannes L. Schestag

Als Ansichtsexemplar genehmigt von

Karlsruhe, den 07.03.2018, _____

Prof. Dr. Anke-Susanne Müller

Contents

List of Figures

1. Introduction

Synchrotron light sources are particle accelerators specifically designed as radiation sources, with equal consideration given to synchrotron radiation production as well as transport and extraction. While they inherit part of their design from the preceding circular electron accelerators used in high energy physics, their purpose is limited to the production of electromagnetic radiation. The spectral range extends from the infrared range, i.e. millimetre radiation over the visible and ultraviolet spectrum down to the nanometre range. At the high frequency limit this enables applications such as X-ray spectroscopy, imaging, scattering and lithography [1].

A subset of this radiation is emitted in the range of 0.3 to 3 THz, the far infrared range. It provides sub-millimetre resolution in imaging applications like microscopy, topography and tomography through a range of dry, dielectric and non-polar surface layers. On the other hand, terahertz radiation is used to study the spectroscopically accessible properties of a wide range of materials of condensed or gaseous phase. This motivates the effort to enhance the power emitted in the form of far infrared radiation in synchrotron light sources.

The intensity of radiation emitted at a given frequency is closely related to the structure of its source due to interference. The simplest charge density modulation necessarily encountered in synchrotrons is the electron bunch. At and below bunch lengths, the phase relations within the radiation fields are coherent. Constructive interference leads to an increase in the energy density of the radiation field. With regard to far infrared radiation, this condition is met for bunch lengths below 1 mm.

An important field of study in synchrotron light sources is therefore related to the dynamical laws governing the formation of bunches and smaller charge density modulations. Here, active external forces in combination with the electromagnetic self-interaction of the electron bunch have to be taken into account [1, 2]. Charge density modulations due to intensity-dependent beam instabilities are researched to generate intense synchrotron light in the far infrared range [3, 4, 5].

To estimate the response of a nonintegrable dynamical system to the variation of a physical parameters, it is often helpful to probe a simplified, numerical model [6]. This thesis aims to extend the simulation tool *Inovesa* [7]. To understand the features seen in THz spectra, the beam can be modelled as a line charge as outlined in chapter 2. The implementation of the RF system noise is detailed in chapter 3. Conclusions are drawn in chapter 4. First, the implementation is checked for self-consistency. Thereafter the influence of noise on a typical use case is discussed.

2. Fundamentals of Accelerator Physics

The observed emission of a synchrotron light source is closely related to the stored line charge density. Beginning from the fundamental principles, this relation will be illustrated. Later in this chapter, phenomena governing the dynamics of the electron bunch are explained in terms of their interaction with the longitudinal phase space, i.e. the space of longitudinal position and energy. This chapter is primarily based on [1].

2.1. Particle Dynamics

2.1.1. Guidance and Acceleration

Particles of electric charge $+e$ in a motion guided by an electric field $\boldsymbol{E}$ and a magnetic field $\boldsymbol{B}$ follow trajectories satisfying the Lorentz force law [1]

$$\boldsymbol{F} = e(\boldsymbol{E} + \boldsymbol{v} \times \boldsymbol{B})\,. \tag{2.1}$$

With respect to the velocity vector $\boldsymbol{v}$, this can be split into a parallel and deflecting contribution

$$\boldsymbol{F} = \underbrace{e\boldsymbol{E}_{\parallel}}_{=\boldsymbol{F}_{\parallel}} + \underbrace{e(\boldsymbol{E}_{\perp} + \boldsymbol{v} \times \boldsymbol{B})}_{=\boldsymbol{F}_{\perp}}\,. \tag{2.2}$$

In the presence of a homogeneous magnetic deflecting field of magnitude $B_{\perp}$ perpendicular to the direction of propagation, the particle moves on a closed circle of radius ρ. Since electric deflecting fields are impracticable for relativistic particle accelerators [1], cyclic accelerator rings are based on this principle.

$$F_{\perp} = \frac{\mathrm{d}p_{\perp}}{\mathrm{d}t} \Leftrightarrow evB_{\perp} = \gamma m\frac{v^2}{\rho} \Leftrightarrow \frac{1}{\rho} = \frac{eB_{\perp}}{\gamma m v}\,. \tag{2.3}$$

Here, γ is the Lorentz factor introduced in the relativistic momentum $p_{\perp}$. The synchrotron is based on a magnetic field tuned to the particle momentum at a constant radius.

Particles of different momenta occupy orbits of slightly different circumference. Restoring a particles transverse position towards an ideal trajectory is referred to as beam guidance. In addition to the extensive magnetic dipole fields, quadrupole magnet fields are used to confine the beam transversely.

The parallel electric field component, on the other hand, changes the kinetic energy E_{Kin} proportional to the difference in γ

$$\Delta E_{\mathrm{Kin}} = \int \boldsymbol{F}\mathrm{d}\boldsymbol{r} = e\int \boldsymbol{E}_{\parallel}\mathrm{d}\boldsymbol{r} = (\gamma_1 - \gamma_0)mc^2\,. \tag{2.4}$$

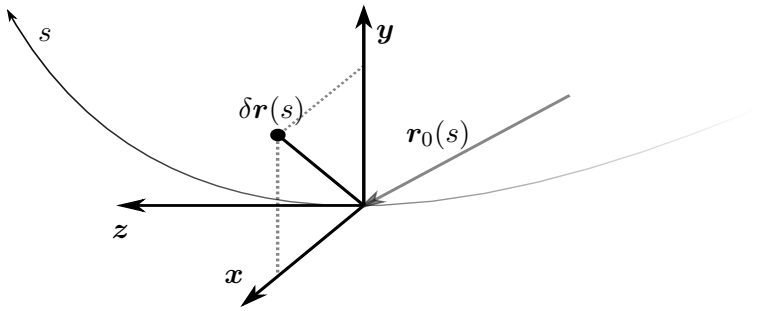

Figure 2.1.: Moving Cartesian coordinate system. Adapted from [1].

In a relativistic particle accelerator, where the particle is moving at a velocity asymptotically close to the speed of light c, this mechanism is referred to as acceleration. It is convenient to use the radial (x), axial (y) and longitudinal (z) directions along a reference orbit as a base of a moving Cartesian coordinate system (Fig. 2.1). Parametrised by the distance s along this orbit, the laboratory particle trajectory is

$$\boldsymbol{r}(s) = \boldsymbol{r}_0(s) + \delta\boldsymbol{r}(s)\,. \tag{2.5}$$

The invariant position with respect to longitudinal beam dynamics, i.e. acceleration, defines the centre of the longitudinal phase space $z = 0$. Energy dependent longitudinal beam dynamics vanishes at the design energy E_0. Only deviations $\mathcal{E} = E - E_0$ have a dynamical response. Sometimes it is convenient to use functions of z and $\mathcal{E}$ to formulate longitudinal dynamics, for example the phase ϕ with respect to the accelerating voltage modulation.

2.2. Synchrotron Radiation

Synchrotron radiation refers to radiation emitted by revolving electrons in storage due to bending at a velocity close to the speed of light in a vacuum. In the laboratory frame of reference related by Lorentz transformation, this radiation is highly collimated in the tangential forward direction. The bulk of radiated power is found in the radiation lobe with opening angle $\approx 1/\gamma$ relative to the direction of travel. Further frequency shifted due to the relativistic Doppler effect, the radiation observed along a bending magnet has a broad power spectrum $p'(\omega)$, depending only the on electron energy $\gamma = E/m_0c^2$ and bending radius. The photon energy band width and high energy contributions are therefore highly sensitive to the electron energy. This can be seen from the Fourier theorem, which relates pulse duration to the photon energy. In theory, the low end of the spectrum observed at a fixed point along a cyclic orbit extends to wavelengths of the circumference of the revolution. This has the practical consequence that the synchrotron spectrum is discrete [8].

Considering a fragmented beam consisting of a large number n_e of electrons in a bunch of length $\sigma_{z,0}$, the spectrum can be divided into qualitatively different domains. Wave lengths comparable to or smaller than the bunch dimensions are radiated in phase, with the entire bunch acting electrically like a point charge. By definition, the power emitted at such a frequency is proportional to n_e^2. This amplification makes coherent synchrotron radiation (CSR) an experimentally attractive spectral feature. In contrast, wave lengths smaller than the bunch are emitted in a random combination of phases, with a power proportional to n_e.

The total power spectrum is the sum of the incoherently amplified single particle contribution p' and the frequency dependent CSR contribution [1]

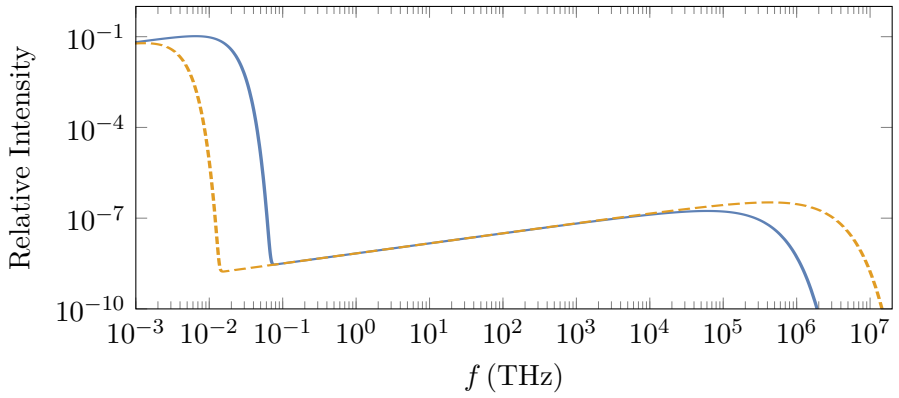

Figure 2.2.: Solid: Exemplary theoretical synchrotron bending spectrum for a Gaussian bunch ($E = 1.3\,\mathrm{GeV}$, $\sigma_{z,0}/c = 10\,\mathrm{ps}$) for a customary bending radius and bunch population. The Gaussian CSR feature is clearly visible at low frequencies ($f < c/\sigma_{z,0}$) on top of a incoherent SR power floor (detailed in [1]). **Dashed:** Spectrum of a larger bunch at higher energy ($E = 2.5\,\mathrm{GeV}$, $\sigma_{z,0}/c = 50\,\mathrm{ps}$).

$$\frac{\mathrm{d}P}{\mathrm{d}\omega} = n_e[1 + (n_e - 1)F(\omega)]\frac{\mathrm{d}p}{\mathrm{d}\omega}\,. \tag{2.6}$$

The longitudinal form factor $F(\omega)$ contains the frequency dependence of the coherent spectrum. For a Gaussian bunch of length $\sigma_{z,0}$, high frequencies are damped exponentially,

$$F(\omega) = \exp\left(-\frac{\omega^2\sigma_{z,0}^2}{c^2}\right). \tag{2.7}$$

The relation between the CSR power for a Gaussian bunch and the THz domain is illustrated in figure 2.2. It suggests that a short enough bunch can be manufactured to significantly improve the THz yield. A length of 1 ps corresponds to the wavelength of THz. This motivates the investigation of the longitudinal dynamics of small and non-Gaussian bunches in synchrotron light sources.

2.3. Zero Current Longitudinal Dynamics

In this section phenomena in the longitudinal phase space of a sparsely populated relativistic electron bunch in storage are introduced. For completeness, some higher order and extremal behaviour of a bunch due to interaction with external forces are discussed.

2.3.1. Momentum Compaction

Consider a charged particle revolving in a magnetic field. Neglecting electromagnetic attenuation, the particle moves under the influence of the Lorentz force on a closed trajectory of integrated length L. Other particles at a different momentum $p+\Delta p$ revolving in the same magnetic field may be ordered by their respective travel $L + \Delta L$. The ratio between their relative path length difference and first order momentum deviation is defined as the momentum compaction α_c,

$$\frac{\Delta L}{L} = \alpha_c\frac{\Delta p}{p}\,. \tag{2.8}$$

This parameter depends on the design of the magnetic provisioning of the orbits ordered by ΔL and is in the context of this thesis always positive. It is generally itself momentum

dependent, so that $\alpha_c = \alpha_0 + \alpha_1 \Delta p/p + \ldots$. With α_c, the time evolution of the time advance τ in terms of the momentum compaction and energy difference $\mathcal{E} = E - E_0$ to the design energy E_0 is given by [9]

$$\dot{\tau} = \frac{1}{\beta^2}\left(\alpha_c - \frac{1}{\gamma^2}\right)\frac{\mathcal{E}}{E_0}\,. \tag{2.9}$$

The $-1/\gamma^2$ term accounts for the influence of the velocity on the revolution period and $\beta = v/c$. At highly relativistic velocities, orbital compaction depending on momentum is predominantly responsible for the reordering of bunch electrons along the longitudinal axis.

The reduction of $\alpha_c - \gamma^{-2}$ translates into a reduced exchange of particles between bunch head and tail. Efforts can be made to reduce α_c by exerting close control over the orbit lengths up to the desired order in $\Delta p/p$. This results in a reduced bunch length at a prevalent energy spread. The operation with quasi-isochronous orbits resulting in $\dot{\tau} = 0$ is difficult because the influence of repeated acceleration accumulates on the energy distribution of the accelerated particles, compromising its long term stability and increasing the influence of achromatic elements used in beam guidance.

2.3.2. Acceleration

Acceleration is the exchange mechanism restoring the kinetic energy lost to synchrotron radiation. Charged particles are accelerated in a electrostatic gradient or in a generic suitable radio frequency (RF) electric mode parallel to the particles velocity. In circular accelerators, particles are accelerated while they traverse a small number of straight accelerating sections of total effective accelerating peak voltage $\hat{V}$. This implies the synchronicity condition on accelerating voltage frequency and travel. To correlate the energy gain in subsequent transits, the revolution time f_0 of a bunch is related to the RF wave modulation by

$$f_{\mathrm{RF}} = h f_0\,. \tag{2.10}$$

The harmonic Number h also limits the number of bunches in circulation at a given time. To reinforce this important relation, the time advance τ associated with a given orbit is translated into a phase difference ϕ_z relative to the alternating accelerating voltage. The time evolution of this phase difference is given by

$$\dot{\phi}_z = -2\pi h f_0 \dot{\tau} = -\frac{2\pi h f_0}{\beta^2}\underbrace{\left(\alpha_c - \frac{1}{\gamma^2}\right)}_{=:\eta}\frac{\mathcal{E}}{E_0}\,. \tag{2.11}$$

With an accelerating RF modulation of a constant frequency, off-momentum particles move on closed trajectories in phase space and perform a stable harmonic oscillation. However, in relativistic electron synchrotrons the electromagnetic dissipation of particle energy is non-negligible. Beam bending magnets and insertion devices are the primary causes for single particle energy loss, other sources like induction heating of the vacuum chamber contribute as well. The stable invariant position of the synchrotron oscillation therefore is the synchronous phase ϕ_s at which a bunch is accelerated to the energy lost during the turn, U_0. It satisfies

$$eV(\phi_s) = e\hat{V}\sin(\phi_s) = U_0\,. \tag{2.12}$$

Any phase excursion ϕ_z added to the synchronous phase or energy surplus $\mathcal{E}$ is linked to a instantaneous change in the relative energy difference $\mathcal{E}$ by

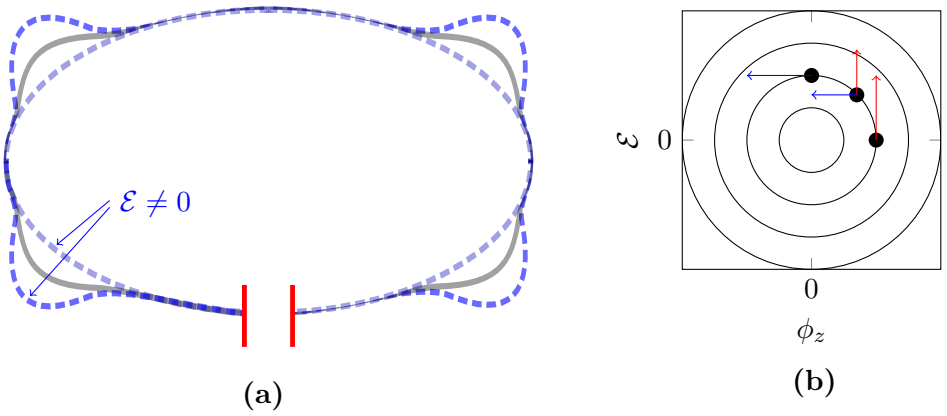

Figure 2.3.: Principle of phase stability. **(a)** Particles with excess energy follow expanded orbits (dashed) and appear slower. **(b)** Phase space of a one dimensional harmonic oscillator illustrating the synchrotron motion of an electron. The scale is chosen to assimilate the magnitude of drift (blue) and acceleration (red arrows). Adapted from [10].

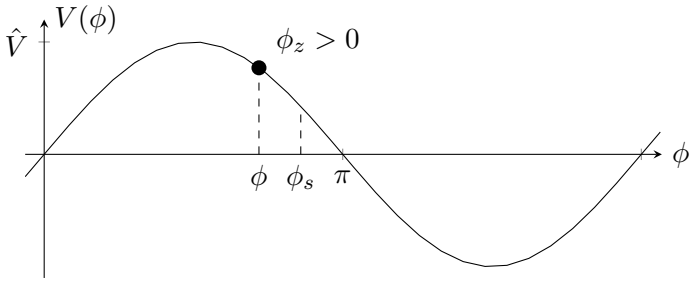

Figure 2.4.: Effective voltage accelerating an electron at (ϕ). Due to the sine modulation, the time delay is roughly proportional to the acceleration voltage.

$$\dot{\mathcal{E}}(\phi_z) \approx e\hat{V} f_0[\sin(\phi_s + \phi_z) - \sin(\phi_s)] - \frac{\mathrm{d}U_0}{\mathrm{d}E} f_0 \mathcal{E}\,. \tag{2.13}$$

The first part is the RF contribution, the second part is a linear radiation damping term. It causes an initial energy fluctuation $\mathcal{E}$ to vanish exponentially over time.

Equations (2.11) and (2.13) determine the time evolution of a coordinate in the two dimensional longitudinal phase space, spanned by a $\mathcal{E}$ and ϕ_z. This motion is called the synchrotron oscillation. Figure 2.3 illustrates this behaviour for single particles and small oscillations. If the number of particles is sizeable enough to form a smooth charge distribution, it rotates at the synchrotron frequency f_s. To define f_s, the slope of the acceleration voltage is taken to be $V'(\phi_s)$ at the bunch centre,

$$f_s^2 = -\frac{h f_0^2 \eta}{2\pi\beta^2 E_0} e \left.\frac{\mathrm{d}V}{\mathrm{d}\phi}\right|_{\phi\approx\phi_s}\,. \tag{2.14}$$

This approximation is qualified by the relatively small bunch size compared to the RF wave as a consequence of radiation damping.

2.3.3. Stochastic Effects

Equation (2.13) introduces radiation damping as a contribution to the time evolution of $\mathcal{E}$. This is a time averaged account relevant for the description of the synchrotron motion. To explain the natural bunch shape, the diffusing character of synchrotron radiation has to be considered as well. Considering the particle nature of the emitted wave packet, the

time evolution of the energy $\mathcal{E}$ is more appropriately described as a biased random process. Radiative damping is generally focusing the bunch by imposing stationarity on the energy excursion amplitude of individual electrons.

Other such processes randomly acting on individual particle with effects are also usually considered in a accumulative manner. Collisions with the residual atmosphere expand the phase space volume occupied by the bunch and cause energy loss. Touschek scattering and intra bunch scattering are phenomena involving the introduction of momentum from oscillations and transitions along orthogonal degrees of freedom into the longitudinal phase space. Such effects may increase the longitudinal beam temperature or compromise the long term beam stability if they exceed the relaxing influence of synchrotron radiation.

These processes are jointly referred to as damping and diffusion. For the electrons in a relativistic synchrotron, radiation damping is the predominant mechanism. This results in the bunch relaxing towards a Gaussian distribution in longitudinal positions and energies. The bunch length is defined as the root mean square displacement from the bunch centre of the Gaussian profile, at zero current given by [1]

$$\sigma_{z,0} = \frac{c|\eta|}{2\pi f_s} \frac{\sigma_{\mathcal{E},0}}{E_0} \,. \tag{2.15}$$

Using the definition (2.14), the bunch length is proportional to $\hat{V}^{-1/2}$ as well as $\alpha_c^{1/2}$. It also depends on the RF slope, which is largest for small ϕ_s. To reduce the bunch length, the accelerating wave is of a high frequency and amplitude. The tradeoff in beam stability is discussed below. In a typical setup the RF wave length covers more than 20 bunch lengths, so that equation (2.14) holds.

The zero current bunch length is only measured in the limit of a vanishing single bunch current, when the self interaction of bunch electrons is not appreciably mediated by CSR and can be neglected.

2.3.4. Separatrix

Figure 2.4 shows the acceleration cavity voltage profile over time. In this example, particles are accelerated at the descending slope, where the potential restoring the electron phase is locally parabolic. To generalise the discussion, the phase space motion for arbitrary initial conditions is plotted in figure 2.5. The phase space depicted here is divided into an area of cyclic motion including $(\phi_z = 0, \mathcal{E} = 0)$ and separating motion. The extremal trajectory associated with a bunch is called the separatrix. The shape and size of the separatrix changes as a function of the synchronous phase, growing with the RF slope.

The synchrotron beam is therefore necessarily bunched. Up to h other bunches may follow enclosed in consecutive separatrix intervals and contribute to the beam. To sustainably store electrons, the volume enclosed by the separatrix is usually at least two orders of magnitude larger than the bunch volume to conserve the bunch occupation under the influence of damping and diffusion over several hours. Consequently, the dynamics of the longitudinal phase space can be adequately treated as harmonic oscillator.

2.3.5. Vlasov-Fokker-Planck-Equation

Solving (2.11) for $\ddot{\phi}_z$ and using (2.13) in the first order reveals the condition for ϕ_z at small angles and energy deviations [1],

$$\ddot{\phi}_z + 2\alpha\dot{\phi}_z + f_s^2\phi_z = 0 \,. \tag{2.16}$$

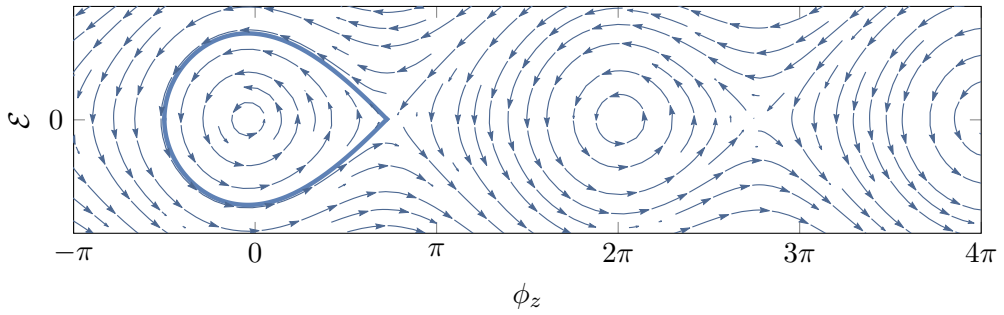

Figure 2.5.: Phase portrait of the synchrotron motion at large phases, $\phi_s = 7\pi/8$. The bunch is confined to a small point at the center of the area enclosed by the separatrix (**solid**). Based on [1].

This is the differential equation of a harmonic oscillator, where the radiation damping parameter α is given by

$$\alpha = -f_0 \frac{1}{2} \left. \frac{\mathrm{d}U_0}{\mathrm{d}E} \right|_{E_0} . \tag{2.17}$$

For positive α this is a generic damped oscillator at small angles. Any set of initial conditions for phase and momentum will relax asymptotically towards the trivial solution $\phi_z = 0$. Acknowledging the stochastic driving forces emerging in the microscopic picture as a boundary condition, equation (2.16) can be extended with a stochastic term to describe an ensemble of non-interacting electrons within a bunched beam. However, in systems with typical electron counts exceeding $n = 10^8$ particles, numerical calculations based on (2.16) with additional collective interactions are not feasible.

The large number of identical particles permits the treatment of the bunch as a continuous distribution of electrons in a two-dimensional phase space. A self consistent description of the longitudinal phase space density of an electron bunch is given in terms of solutions $\psi(q, p, t)$ satisfying the Vlasov-Fokker-Planck-equation,

$$\frac{\partial \psi}{\partial t} + \frac{\partial H}{\partial p}\frac{\partial \psi}{\partial q} + \frac{\partial H}{\partial q}\frac{\partial \psi}{\partial p} = \beta \frac{\partial}{\partial p}\left(p\psi + \frac{\partial \psi}{\partial p} \right) . \tag{2.18}$$

Here, H is the Hamiltonian of the undamped harmonic oscillation along $q = z/\sigma_{z,0}$ with conjugate momentum $p = (E - E_0)/\sigma_{\mathcal{E},0}$. The right hand side is called the Fokker-Planck contribution. Broadly speaking, the energy dependent part restores the mean energy and the shape dependent part is responsible for clustering of the bunch. It accounts for the stochastic process of incoherent radiation damping, parametrised with β.

Nontrivial closed phase space density solutions of the VFPE are available for small perturbations to H due to collective effects. If the perturbation is large, it can be evaluated numerically to simulate the time dependent behaviour of intense beams.

2.4. Collective Longitudinal Dynamics

To discuss productive applications of beam instabilities in the production of radiation, intensity dependent beam instabilities have to be taken into account [1]. The term intensity can be properly defined using a versatile scaling function. In the context of this thesis, transitions between intensity domains involve only the bunch charge. It is understood that the transition occurs in a number of dimensions.

At non-negligible intensities, the bunch electrons will be subjected to additional potentials due to the interaction with its own coherent synchrotron radiation. The total Hamiltonian function governing the dynamics of a particle located at a phase ϕ_z can be written as [7]

$$H_{\text{total}}(\phi_z) = H_0(\phi_z) + H_{\text{wake}}(\phi_z, \tilde{\rho}(t))\,. \tag{2.19}$$

The intensity dependence is contained within the wake Hamilton function H_{wake}, which is the potential energy of a bunch electron due to the bunch charge distribution mediated by CSR.

This kind of self-interaction within the particle beam is quantified by a longitudinal impedance $Z_{\parallel}$. In this context, the impedance is due to boundary conditions on the emission of radiation. In the free space approximation, the curved nature of the orbit allows the oriented exchange of radiation within the bunch from tail to head along chords.

A more realistic picture of a synchrotron includes parts of the narrow, conducting vacuum chamber surface acting as a high pass filter and delay. The shielding cut off frequency associated with a simple impedance can be approximated analytically. There are broad band impedances associated with all types of electromagnetic constriction of the aperture within customary beam guides. For example, higher order excitations of the accelerating cavity field by the passing bunch cannot be completely avoided. This enables CSR to propagate across the bunch in both longitudinal directions. Such structures may also sustain a resonant mode fairly long and serve to couple different bunches at long range. The potential energy due to the exchange of CSR is characterised using the impedance [1]

$$V_{\text{wake}}(\phi_s) = \mathscr{F}\Big\{ Z_{\parallel}(\omega)\tilde{\rho}(\omega) \Big\}(\phi_s)\,. \tag{2.20}$$

$\mathscr{F}$ denotes the Fourier transform.

At moderate beam intensities, the potential in (2.19) causes a perturbative potential well distortion and the bunch to lengthen. Conversely, measurable bunch lengthening may be used to quantify the effective impedance of an inhomogeneous array of wave guides. Depending on the nature of the impedance, this may lead to an asymmetry in the longitudinal density. This is referred to as a Haïssinski-equilibrium, a non-Gaussian steady state, closed solution of the nonlinear VFPE.

2.4.1. The Microbunching Instability

Collective interactions throughout the bunch at high intensities lead to this phenomenon, the result of a positive feedback loop in the dynamics of a intense beam. The energy modulation H_{wake} grows with the bunch charge. The discussion of longitudinal beam dynamics so far shows that this leads to a modulation of the longitudinal bunch profile. However, above the microbunching threshold intensity there is no steady state potential well distortion. The small distortion to the bunch profile is then contributing moderate high frequency spectral components. CSR at these frequencies is far less subject to shielding and intensifies under the influence of its growing wake forces. The profile develops pronounced sub-structures. Accordingly, the longitudinal form factor (2.7), exhibits significant side lobes at the frequencies corresponding to these sub-structures. The nonlinear growth in power radiated coherently by a subset of bunch electrons however results in a situation that is adverse to the enabling initial condition of a local narrow CSR excitation. Measurable bunch lengthening is a diagnostic signal to determine the bursting threshold. Without the diffusing effect of microbunching, the bunch length is again dominated by damping and will contract. This cycle, recurring at time scales of the damping time, is called a CSR burst.

A distinctive special case of bursting is found in the transitional intensity regime above the bursting threshold. In this current domain, the power emitted during the burst is modulated with a highly regular cadence. This is due to the continuous appearance of harmonically rotating structures in phase space.

At very high intensities, sub-structures appear without the same regularity. Due to the complex time structure of the bursting onset, this is referred to as sawtooth bursting.

2.5. Synchrotron Oscillation Driven by RF Noise

Particle acceleration as introduced above generally involves small perturbations. The physical infrastructure used to generate, amplify and transport the RF wave will produce a waveform that is stable only up to the effective peak amplitude and frequency. High frequency voltage modulations originate from thermal fluctuations. Mechanical vibrations contribute lower frequency modulations and noise [11].

Here, the instabilities are assumed to introduce white Gaussian noise w of a given amplitude σ. One assumption is that the noise is zero mean, $\langle w(t)\rangle = 0$. The autocorrelation, defined as the correlation of w with itself at different times, is required to vanish. With the Dirac-δ function it is written as:

$$R(\tau) = \langle w(t)w(t+\tau)\rangle = \sigma^2\delta(\tau)\,. \tag{2.21}$$

To implement a white noise process in a numerical simulation, its variance σ^2 has to be interpreted with respect to a frequency, for example the revolution frequency f_0 [12]. This will be discussed in chapter 3.

Here, the influence of Gaussian noise in each variable with an amplitude parameter is discussed analogous to [13].

2.5.1. Amplitude Noise

The mean peak voltage $\hat{V}$ is subject to random fluctuation of amplitude $\sigma_{\hat{V}}$, defined for a given time or number of cycles. It manifests as an adjustment $\delta V(t)$ to the oscillation amplitude. The mean acceleration voltage throughout the bunch is affected with

$$\sigma_V = \left|\frac{\partial V}{\partial \hat{V}}\right|\sigma_{\hat{V}} = |\sin(\phi_s)|\sigma_{\hat{V}}\,. \tag{2.22}$$

This situation is shown in figure 2.6. The fluctuation of the RF slope is reflected in the synchrotron frequency (2.14):

$$\sigma_{V'} = \left|\frac{\partial}{\partial \hat{V}}\left(\left.\frac{\mathrm{d}V}{\mathrm{d}\phi}\right|_{\phi_s}\right)\right|\sigma_{\hat{V}} = |\cos(\phi_s)|\sigma_{\hat{V}}\,. \tag{2.23}$$

At very small synchronous angles the instability of the RF amplitude is visible only as a contribution to the instantaneous synchrotron frequency.

2.5.2. Phase Noise

The acceleration due to Phase noise can be derived similar to the case of amplitude noise. Again, $\sigma_{\phi s}$ is understood to be the amplitude of the shift in synchronous phase $\delta\phi_s(t)$ for a

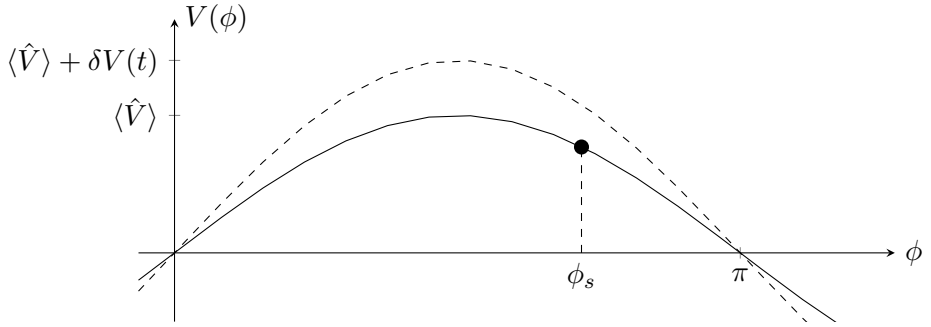

Figure 2.6.: RF modulation mean (**solid**) and with amplitude variation (**dashed**). For $\phi_s \to \pi$, the instability becomes purely multiplicative.

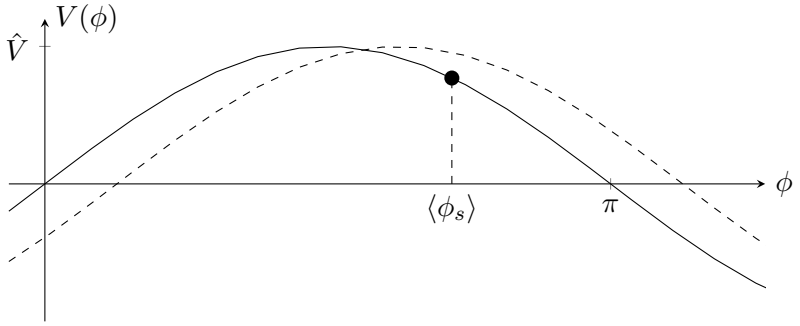

Figure 2.7.: RF modulation, mean (**solid**) and phase shifted (**dashed**). ϕ_s is effectively shifted to $\phi_s < \langle\phi_s\rangle$. For $\langle\phi_s\rangle \to \pi$, the instability becomes purely additive.

given number of RF cycles. The same treatment applies for zeroth and first order of the RF wave (Fig. 2.7).

$$\sigma_V = \left|\frac{\partial V}{\partial \phi_s}\right|\sigma_{\phi s} = \left|\hat{V}\cos\left(\phi_s\right)\right|\sigma_{\phi s}\,. \tag{2.24a}$$

$$\sigma_{V'} = \left|\frac{\partial}{\partial \phi_s}\left(\left.\frac{\mathrm{d}V}{\mathrm{d}\phi}\right|_{\phi_s}\right)\right|\sigma_{\phi s} = \left|\hat{V}\sin\left(\phi_s\right)\right|\sigma_{\phi s}\,. \tag{2.24b}$$

2.5.3. Multiplicative RF Noise

The amplitude of the perturbations (2.23) and (2.24b) are summed up to the instability in f_s. It is therefore referred to as multiplicative noise, changing the dynamics in the first order without affecting the mean energy of the bunch. Assuming small, uncorrelated errors,

$$\frac{\sigma_{f_s}}{f_s} = \frac{1}{f_s}\left|\frac{\partial f_s}{\partial V'}\right|\sigma_{V'} = \frac{1}{2}\frac{\sigma_{V'}}{|V'|} = \frac{1}{2}\frac{\sqrt{\left|\cos\left(\phi_s\right)\right|^2\sigma_{\hat{V}}^2 + \left|\hat{V}\sin\left(\phi_s\right)\right|^2\sigma_{\phi s}^2}}{\left|\hat{V}\cos\left(\phi_s\right)\right|} \tag{2.25}$$

At $\phi_s' = \pi - \phi_s \ll \frac{\pi}{2}$, the leading order contribution is

$$\left.\frac{\sigma_{f_s}}{f_s}\right|_{\phi_s' \ll \frac{\pi}{2}} \approx \frac{1}{2}\frac{\sigma_{\hat{V}}}{\hat{V}}\,. \tag{2.26}$$

At small synchrotron angles, multiplicative noise is approximated by its amplitude instability contribution.

2.5.4. Additive RF Noise

Using the acceleration contribution of equation (2.13), the noise contribution to acceleration at $\phi_z = 0$ is given by the sum of (2.22) and (2.24a):

$$\sigma_{\dot{\mathcal{E}}} = e\sigma_V = e\sqrt{\left|\sin\left(\phi_s\right)\right|^2\sigma_{\hat{V}}^2 + \left|\hat{V}\cos\left(\phi_s\right)\right|^2\sigma_{\phi s}^2}\,. \tag{2.27}$$

In leading order of ϕ_s' at synchrotron angles $\phi_s' \ll \frac{\pi}{2}$ this is

$$\sigma_{\dot{\mathcal{E}}}\big|_{\phi_s' \ll \frac{\pi}{2}} \approx e\hat{V}\sigma_{\phi s}\,. \tag{2.28}$$

Additive RF noise is dominated by its phase instability contribution.

3. Implementation of the RF Instability

3.1. Introduction to *Inovesa*

The *Inovesa* Numerical Optimized Vlasov-Equation Solver (*Inovesa*) has been published by Schönfeld et al. in March 2017 [7]. The source code of the development version is available at GitHub[1] with an open-source license. Among its distinguishing features is a graphical user interface and support for heterogeneous processing using OpenCL.

At the core of *Inovesa* is a simulation of the longitudinal phase space based on the numerical integration of the Vlasov equation (2.18). The simulation of the CSR wake field provides the functionality necessary to simulate features of the CSR signature of the microbunching instability beyond what is possible in terms of closed solutions. *Inovesa*'s predictive capabilities have been assessed phenomenologically at the synchrotron *Karlsruhe Research Accelerator*. The anticipated degree of microbunching, i.e. cluster formation in phase space has been reproduced. The minimal intensity threshold at which microbunching occurs agrees well with measurement and theory. However, the accuracy is inherently limited by the deliberate generality of the model even before considering numerical effects.

These idealisation compromises include the perfect homogeneity of the beam container consisting of two perfectly conducting plates of infinite extent. With the electron bunch revolving on circles in the midplane, the impedance is exhaustively parametrised by the orbit radius and separation of the plates G. The description in terms of the electric field has been derived by Murphy et al [14]. Effects of the CSR beam line, i.e. the transport system connecting a detector with the beam guide tangentially from the source point, on the radiation are beyond the scope of the simulation. The RF system is linearised, i.e. the associated potential well is parabolic. For a straightforward account of the RF noise, the mathematical model is extended to set the idealised synchrotron phase to $\phi_s = 2\pi$.

The mathematical model of the physical system is then discretised, i.e. broken down into finite elements, here uniform steps of time and Cartesian space. Continuous physical quantities are windowed and sampled. In this step, computer simulations inevitably introduce errors due to precision limits inherited from the native capabilities of the underlying hardware. All artificial parameters arising from discretisation have to be chosen within their stability and convergence boundaries. With some limitations, these errors are mitigated by the choice of an advantageous formulation of the mathematical model. Within the VFP equation (2.18), special consideration has to be given to the Vlasov contribution. The *Inovesa* discretisation model is an extension of Warnock and Ellison [6], making use of repeated operator splitting. First, the harmonic oscillation is included as a rigid rotation in phase space of fixed step size. Secondly, the influence of the time dependent wake force on the bunch energy is considered. The residual numerical effect on the total bunch charge can be mitigated by periodic renormalisation. These numerical influences have to be accounted for when interpreting *Inovesa* results.

[1] `https://github.com/Inovesa/Inovesa`

The two dimensional phase space density as a function of the normalised coordinates is given by

$$\psi(q,p,t),\ q=\frac{z}{\sigma_{z,0}},\ p=\frac{\mathcal{E}}{\sigma_{\mathcal{E},0}}\,. \tag{3.1}$$

A coordinate transformation conveniently maps an interval $[q_{\min}, q_{\max}]$ on a positive grid coordinate x

$$x(q)=(q-q_{\min})\frac{x_{\max}}{q_{\max}-q_{\min}}=\frac{q-q_{\min}}{\Delta q}\,. \tag{3.2}$$

The analogous transformation is applied on p to get $y=(p-p_{\min})/\Delta p$. The positive integers $x_{\max}, y_{\max}$ define the grid extension used to uniformly sample and store the phase space density during each iteration step.

Another parameter appearing in the derivation of the discrete model is the simulation time step δt. This is set to a small fraction $1/N$ of the phenomenologically relevant time constant $T_s = 1/f_s$ in the mathematical model. The time step is given by

$$\delta t=\frac{1}{N f_s}\,. \tag{3.3}$$

Consequently, the time step rotates the phase space by an angle θ

$$\theta=\omega_s\delta t=\frac{2\pi}{N}\,. \tag{3.4}$$

The mathematical rotation step in *Inovesa* is split to separate the dynamical effects of momentum compaction and the RF cavity. As a numerical approximation to a infinitesimal rotation, this is not immediately related to the alternating nature of the longitudinal dynamics as they have been introduced above. The mathematical model assumes cylindrical symmetry of the synchrotron model and therefore a simultaneous action of acceleration and drift. However, this is a numerically advantageous practice since the canonical coordinates in the Hamiltonian are Cartesian.

3.1.1. Evaluation and Interpretation of *Inovesa* Results

Inovesa saves uniformly spaced samples of diagnostic information into a HDF5 file, a tree of homogeneous arrays. In addition, ancillary data containing the parametrisation and metadata is available. Sampled quantities include the instantaneous CSR intensity as well as the bunch profile and position.

3.1.1.1. CSR Power

As a system response of diagnostic relevance, *Inovesa* continuously records the CSR power loss. Incoherent radiation and resistive wall effects are not considered. The emission is calculated using the dissipative part of the *Inovesa* Impedance [7]

$$P(t)\propto\int_0^\infty \mathrm{Re}\Big[Z_\parallel(\omega)\Big]\cdot|\tilde{\rho}(\omega,t)|^2\mathrm{d}\omega\,. \tag{3.5}$$

3.1.1.2. Bursting Spectrogram

The bursting spectrogram serves as a visualisation of slow CSR frequency content, referred to as modulations. These indicate indirectly the threshold behaviour of intensity dependent beam instabilities. A bursting spectrum is obtained by discrete Fourier analysis of the simulated total CSR power emission under a adiabatic variation of an intensity parameter. Transient phenomena following a correction have to be cut. In a subsequent synthesis, spectra obtained at different parameter values build up the bursting spectrogram. A customary choice of parameter is the number of electrons in a bunch, proportional to the bunch current at a given revolution frequency.

For a *Inovesa* CSR intensity $c_j(t)$, $t = 0, 1, .., N-1$ recorded at the j-th decrement of a bunch current $j = 0, .., K-1$, the spectral intensity $\tilde{c}_j(f)$ is given by the discrete Fourier transform

$$\tilde{c}_j(f) = j^2 \left| \sum_{t=0}^{N-1} e^{-2\pi i \frac{ft}{N}} c_j(t) \right|, \; f = 0, ..., N-1 \,. \tag{3.6}$$

The bursting spectrogram is the matrix consisting of rows of $\tilde{c}_j$:

$$(\mathrm{s}) = \begin{pmatrix} \tilde{c}_0(1) & \tilde{c}_0(2) & \dots & \tilde{c}_0(N/2) \\ \tilde{c}_1(1) & \ddots & & \vdots \\ \vdots & & & \\ \tilde{c}_{K-1}(1) & \dots & & \tilde{c}_{K-1}(N/2) \end{pmatrix} . \tag{3.7}$$

This is illustrated in Fig. 3.1 for measurement [15] and simulation. The presentation is improved by applying colours on a logarithmic scale.

Between the high and low intensity areas filling the top and the bottom is the regular bursting regime, signified by the presence of pronounced structure. An important detail characteristic for this interval the is the finger, a bursting modulation attributable to a particularly regular occurrence of microstructures in phase space discussed above. The tilted shape reveals that the repetition rate of these structures is a function of the bunch current. At the low current limit, close to 0.2 mA, reducing the current causes a sudden drop in emitted CSR power as the bunch converges to the Haïssinski-equilibrium. Increasing the current causes the bunch to continuously assume the bursting pattern with a sawtooth envelope. The character of the bursting envelope is crudely captured in the low frequency content near 0 Hz. The DC contribution is clipped in the interest of the presentation.

3.2. Discrete model of RF Noise

Until now, the boundary condition on the RF instability was discussed in terms of the respective noise Amplitudes $\sigma_{\hat{V}}$ and $\sigma_{\phi s}$. In experimental applications of RF acceleration, these parameters may be attributes of individual accelerating sections. In *Inovesa*, accelerating sections are conceptualised as the driving force behind the continuous synchrotron rotation. The actual number of synchrotron rotation steps per revolution period is derived from artificial parameters and lacks a physical interpretation. Since the discretisation should be transparent, the response of the simulation can only depend on physical constants.

With regard to a numerical integration of the VFPE using finite time steps, it is necessary to physically interpret the Gaussian white noise term $w(t)$ and the property (2.21). Allowing for the above motivated degree of autocorrelation, the effective fluctuation w_n for the n-th

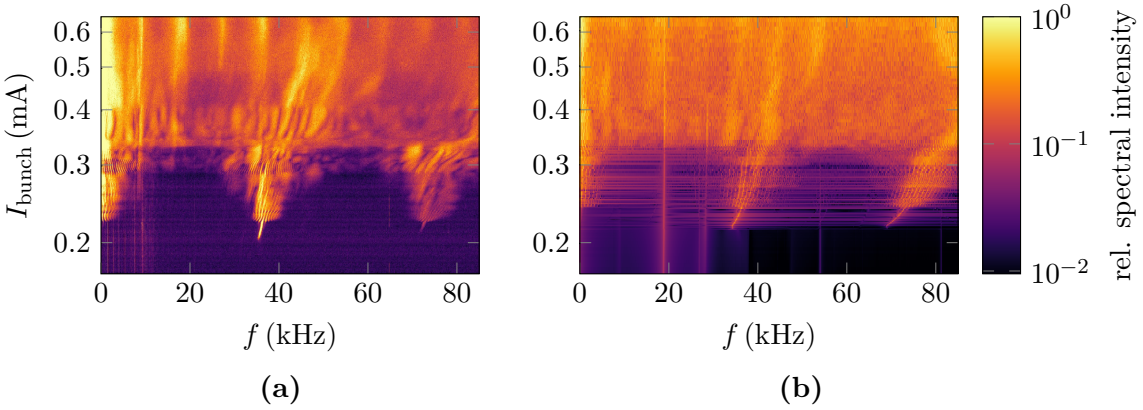

Figure 3.1.: Measured bursting spectrogram **(a)** and a reproduction in *Inovesa* **(b)**. The experimental data is based on the THz power emitted by the *Karlsruhe Research Accelerator* at $f_s \approx 8.9\,\text{kHz}$ (found similiarly in [7]). *Inovesa* predicts the bursting threshold in the form of a regular modulation with a $\approx 4\,f_s$ cadence. Slightly above the threshold, the progressive onset of a sawtooth modulation is responsible for a diffusion of the modulation across a widening frequency band. The $2f_s$ modulation in the Haïssinski-domain visible in the simulated spectrogram is a numerical artefact, since the phase space density below the threshold is constant in the absence of physical noise.

revolution is defined as a noise of finite amplitude. The w_n follow a Gaussian distribution of amplitude σ

$$w_n \sim \mathcal{N}(0, \sigma)\,. \tag{3.8}$$

The equivalent noise function for a different time interval δt is w'. As a consequence of the propagation of uncertainty, the w' also follow a Gaussian distribution,

$$w' \sim \mathcal{N}\left(0, \sigma' = \sqrt{\frac{\delta t}{T_0}}\sigma\right). \tag{3.9}$$

It is useful to define the fractional revolution number $\mathfrak{f}$ as

$$\mathfrak{f} = \frac{\delta t}{T_0}\,. \tag{3.10}$$

This allows the transformation of general instability amplitudes into effective amplitudes per simulation step δt. A stochastic contribution to the acceleration $\delta\mathcal{E}$ translates into a instability in discrete simulation time as

$$\sigma'_{\delta\mathcal{E}} = \sqrt{\mathfrak{f}}\;\sigma_{\delta\mathcal{E}}\,. \tag{3.11}$$

The bandwidth of band limited white noise is is the inverse sampling interval $\delta t^{-1} = f_s N$ [12], whereas the frequency response of the synchrotron oscillation vanishes rapidly for $f > f_s$ [13].

3.3. Implementation of the *Inovesa* Iteration Step

The phase space $\psi_t(x, y)$ is efficiently iterated repeating a number of interleaved atomic Steps. In *Inovesa*, each logical unit queued in the total time step provides a common

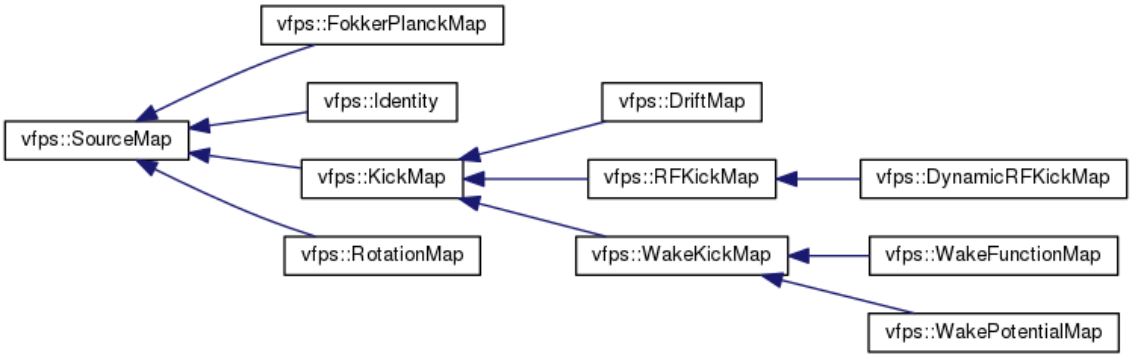

Figure 3.2.: Inheritance diagram showing possible constituents of the iteration step. A default work flow uses a `WakeMap`, the `DriftMap` and `RFKickMap` and the `FokkerPlanckMap` objects.

interface `SourceMap`. Derived from the VFPE, this includes the Fokker-Planck contribution and the three remaining terms accounting for drift, RF kick and kick associated with the CSR wake field. In the Cartesian simulation space, they share an underlying description in the `KickMap`. In physical analogy to the nonlinear term applied in `WakeKickMap`, `RFKickMap` shifts the bunch along the energy coordinate as a function of the longitudinal position. This relation is illustrated in Fig. 3.2. A total simulation step may be serialised to read

$$\ldots \to \texttt{WakeMap} \to \texttt{DriftMap} \to \texttt{RFKickMap} \to \texttt{FokkerPlanckMap} \to \ldots \tag{3.12}$$

Each atomic simulation step is executed once per grid node. The density of the grid nodes has to be chosen under consideration of the execution time. Experience shows that twenty or more grid nodes per bunch length are sufficient to accurately reproduce microbunching in most cases. Usually the output phase space density at a node is an algorithm dependent on the phase space density between nodes. In this case, the phase space density is reconstructed by polynomial interpolation.

The `RFKickMap` translates the phase space distribution along the energy axis analogous to the rotation by θ,

$$\Delta y(x) = (x - x_0) \tan\theta \,. \tag{3.13}$$

Here, x_0 is defined as the regular invariant position of the phase space at the bunch centre of mass. By construction, the virtual RF kick is a finite approximation of the infinitesimal equation (2.13),

$$\delta\mathcal{E} = f_0 \delta t e \hat{V} \phi \,. \tag{3.14}$$

3.4. Implementation of the RF noise

The dynamical influence of RF noise has been discussed in section 2.5. In the following, the results (2.26) and (2.28) are applied to the *Inovesa* iteration step (3.13) using the interpretation (3.11). The multiplicative noise associated with the peak voltage instability shifts the rotation angle increment

$$\sigma_\theta = \sqrt{\mathfrak{f}} \left| \frac{\partial\theta}{\partial f_s} \right| \sigma_{f_s} = \sqrt{\mathfrak{f}} \omega_s \delta t \frac{1}{2} \frac{\sigma_{\hat{V}}}{\hat{V}} = \sqrt{\mathfrak{f}} \theta \frac{1}{2} \frac{\sigma_{\hat{V}}}{\hat{V}} \,. \tag{3.15}$$

The amplitude is transformed using the discretisation provision (3.11). With the definition of the y-axis analogous to (3.2), the amplitude of the instability in the displacement $\Delta y(x)$ is given by

$$\sigma_{\Delta y^\times}(x) = \left|\frac{\partial \Delta y}{\partial \theta}\right|\sigma_\theta = \left|(x - x_0)\tan\theta\left(\frac{\theta}{\cos\theta\sin\theta}\right)\right|\sqrt{\mathfrak{f}}\frac{1}{2}\frac{\sigma_{\hat{V}}}{\hat{V}}\,. \tag{3.16a}$$

$$\sigma_{\Delta y^\times}(x)\Big|_{\theta \ll \frac{\pi}{2}} \approx |(x - x_0)\tan\theta|\sqrt{\mathfrak{f}}\frac{1}{2}\frac{\sigma_{\hat{V}}}{\hat{V}} \tag{3.16b}$$

$$= |\Delta y(x)|\sqrt{\mathfrak{f}}\frac{1}{2}\frac{\sigma_{\hat{V}}}{\hat{V}}\,. \tag{3.16c}$$

Using (2.28), (3.11) and (3.2), the additive y displacement due to a phase instability is, using analogous small angle approximations, given by

$$\sigma_{\Delta y^+} = \sqrt{\mathfrak{f}}\frac{e\hat{V}}{\sigma_{\mathcal{E},0}\Delta p}\sigma_{\phi s}\,. \tag{3.17}$$

The class `DynamicRFKickMap` has been created to multiply and add random samples from a Gaussian distribution of standard deviations $\sigma_{\Delta y^\times}$ and $\sigma_{\Delta y^+}$ to the constant rotation half-step. Two random variates are generated using standard library functions and applied with each evaluation of the `apply()` member. Analogous to (3.13), the implemented stochastic rotation step is

$$\Delta y'(x) = \Delta y(x)[1 + \delta_{\text{mul}}] + \delta_{\text{add}}\,. \tag{3.18}$$

The random variates δ_{mul} and δ_{add} are samples generated by sampling Gaussian distributions of different standard deviations,

$$\delta_{\text{mul}} \sim \mathcal{N}\left(0, \sqrt{\mathfrak{f}}\frac{1}{2}\frac{\sigma_{\hat{V}}}{\hat{V}}\right), \tag{3.19a}$$

$$\delta_{\text{add}} \sim \mathcal{N}\left(0, \sqrt{\mathfrak{f}}\frac{e\hat{V}}{\sigma_{\mathcal{E},0}\Delta p}\sigma_{\phi s}\right). \tag{3.19b}$$

The relevant source code is made available in the official *Inovesa* repository above.

3.5. Usage

The noise is parametrised by specifying command line arguments. Input noise amplitudes are defined as described above and in relation to their physical response described below. By design, the physical response is that to an equivalent instability in a single cavity accelerator.

Physical Parameter	Option	Default	Unit
$\sigma_{\phi s}$	`--RFPhaseSpread`	0	1 °
$\sigma_{\hat{V}}/\hat{V}$	`--RFAmplitudeSpread`	0	1

Inovesa also implements `RotationMap`, an optional fast unification of `DriftMap` and `RFKickMap`. `DynamicRFKickMap` is only available using the composite rotation algorithm referred to as *Manhattan rotation* in *Inovesa*.

4. Evaluation and Results

This chapter summarises the physical results of the RF instability in *Inovesa*. The resilience of the implementation with respect to changes in some artificial parameters is tested in Appendix B.

4.1. Synchrotron Oscillation in Inovesa

Driven by RF phase noise, the bunch centre is generally found to oscillate in phase space. The longitudinal reversal point amplitudes $\hat{\phi}$ are as the response to a stochastic process themselves distributed like random variates. This is physically analogous to the interaction of single electrons with elementary radiation packets. Again, radiation damping prevents the bunch from reaching arbitrarily large phase excursions. An illustrative example of superposed longitudinal motion is given in Fig. 4.1. In addition to the harmonic movement, the bunch exhibits stochastic changes in oscillation amplitude with a broad modulation spectrum.

Although the origin and nature of the perturbation in synchrotron light sources are more involved, the resulting oscillation of the bunch position can be quantified by measurement. A customary method is based on the interaction of the bunch's electric field with a crystal, the variable optical properties of which are synchronously sampled using a laser pulse [16]. This reveals the longitudinal charge distribution and its longitudinal displacement at sub-ps resolution for every turn. Data as represented in Fig. 4.2 allows the reconstruction of the bunch position delay attributable to the coherent synchrotron oscillation.

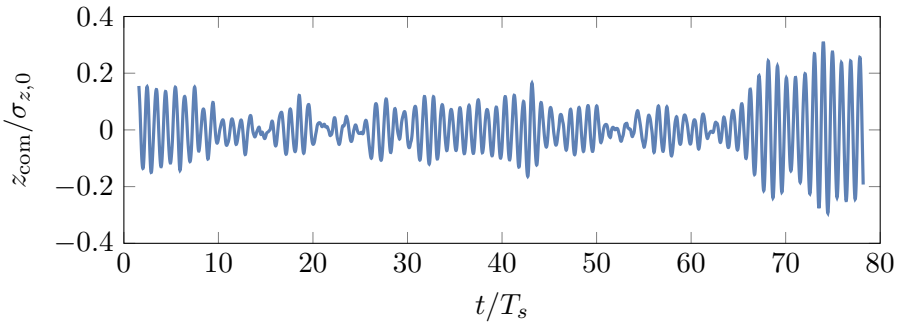

Figure 4.1.: Bunch Position over time in an example *Inovesa* simulation. The oscillation at the resonant frequency f_s is randomly modulated in amplitude.

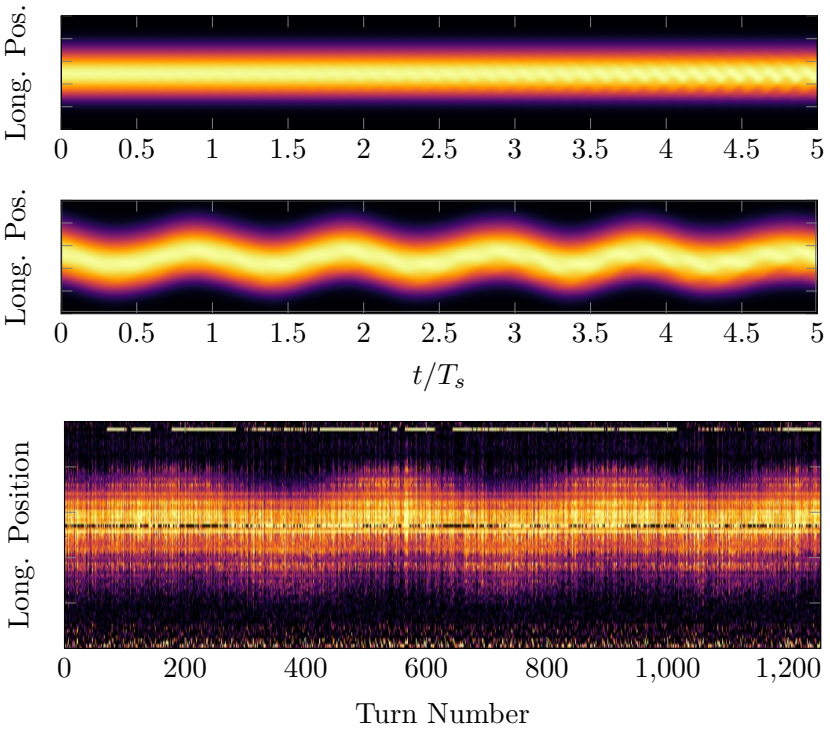

Figure 4.2.:
Top and Middle: The longitudinal charge distribution in an *Inovesa* simulation without and with a coherent synchrotron oscillation due to RF noise.
Bottom: Measurement of the longitudinal charge distribution in consecutive turns. Bright colours indicate a higher electron density at a given longitudinal position (vertical axis), recorded in uniform intervals over multiple revolutions (horizontal axis) at a sampling frequency of 2.7 MHz. Due to the high spatial and temporal stability of the detector, the coherent synchrotron oscillation is visualised as a oscillation of period $T_s \approx 400 T_0$. The vertical axis depicts the actual displacement as it relates to the bunch length [17].

4.1.1. Mean Square Response of the Bunch Position

A closed form for the mean square response $\langle \phi^2 \rangle$ of the phase excursion amplitude is given in [13] in terms of the spectral density near the resonance. In this case, the constant spectral density is (App. A)

$$S \approx \frac{\sigma_{\phi s}^2}{2\pi f_0} \,. \tag{4.1}$$

The mean square response is

$$\left\langle \phi^2 \right\rangle = \pi^2 \frac{f_s^2 \sigma_{\phi s}^2 \tau_d}{f_0} \,. \tag{4.2}$$

Due to the internal representation of the longitudinal phase space, the dependence on f_s^2 is not expected to be exact. Likewise, the simulation fidelity depends on the ratio of τ and the simulation time step δt. To evaluate the mean square response (4.2) in the simulation, the function parameters have been varied individually around a set of centre values given by

$$f_0 = 9\,\mathrm{MHz},\ f_s = 45\,\mathrm{kHz},\ \sigma_{\phi s} = 2\,\mathrm{mrad},\ \tau_d = 1\,\mathrm{ms}\,. \tag{4.3}$$

Results are plotted in Fig. 4.3, the monomial fit functions with a constant term have been selected according to (4.2). The simulation is run for a time of $100\,T_s$ at the default values, detailed in Appendix C.1. Statistical errors are eliminated using a constant seed strategy for the RF noise, and nonlinearities in the VFPE have been neglected. Under these conditions, equation (4.2) predicts the leading order behaviour accurately. The reliability in a simulation with respect to a unique set of artificial and physical parameters has to be assessed individually.

A single long simulation over $t = 10000\,T_s$ with the same parameters has been run and partitioned to estimate the spread to be expected in a typical run. Depending on the partitioning of the long record into short intervals, neighbouring residuals in a linear regression of $\langle \phi^2 \rangle$ over time may be correlated. A generic test for autocorrelation [18] indicates a vanishing first order autocorrelation for partitions spanning times longer than $t = 50\,T_s \approx \tau_d$. At times $t \gg \tau_d$ it is safe to assume that the initial condition is no longer sampled.

4.1.2. Example

The standard deviation of $\langle \phi^2 \rangle$ was found to be large in the simulation of the bursting behaviour below, where the calculated mean square response $\langle \phi^2 \rangle = 1.97 \cdot 10^{-5}\,\mathrm{rad}^2$ for $n = 151$ simulation runs over $t \approx 1.7\,\tau_d$ each was found to be

$$\left\langle \phi^2 \right\rangle_{\mathrm{sim}} = (2.02 \pm 1.39) \cdot 10^{-5}\,\mathrm{rad}^2\,. \tag{4.4}$$

In conclusion, equation (4.2) is suited to estimate the order of magnitude of the oscillatory response. This result also serves as a indication of the self-consistency of the implementation.

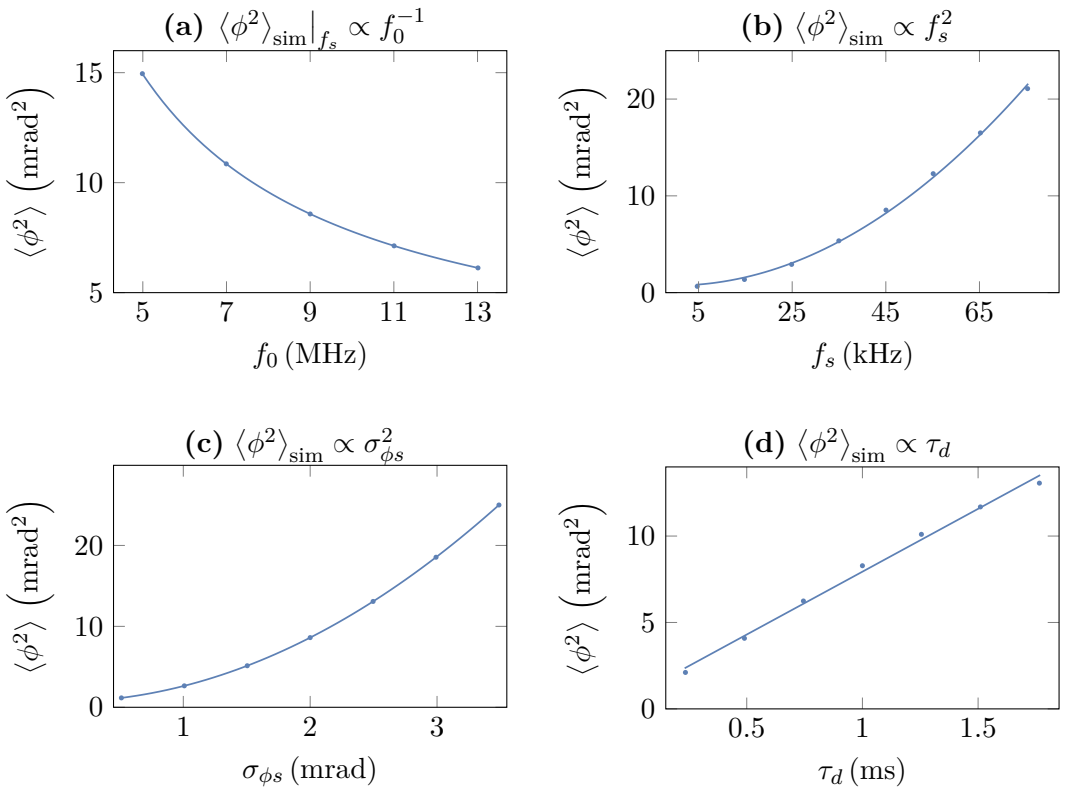

Figure 4.3.: Mean square response of the synchrotron oscillation phase $\langle\phi^2\rangle$ of the bunch centre of mass as a function of a parameter variation in *Inovesa*. The fit function largely exhibit the expected dependencies in the domain up to twice the default value. The constant order behaviour is evaluated separately. **(d)** is evaluated in more detail in Fig. 4.4.

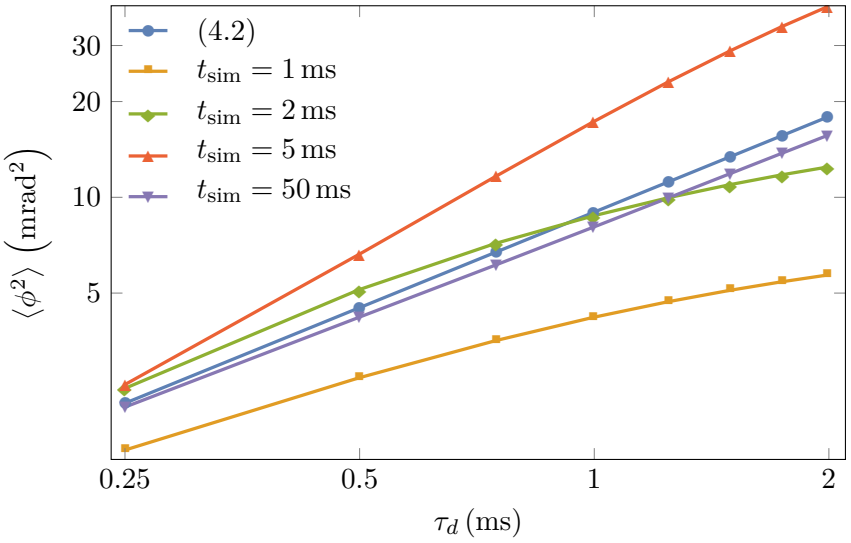

Figure 4.4.: Example of the convergence of $\langle\phi^2\rangle$ over the duration of a simulation. For short simulation times the relation is nonlinear since the initial oscillation amplitude is not sufficiently damped. At $t_{\text{sim}} = 5\,\text{ms}$ the relation approaches linearity, at $t_{\text{sim}} = 50\,\text{ms}$ the simulation response is close to (4.2).

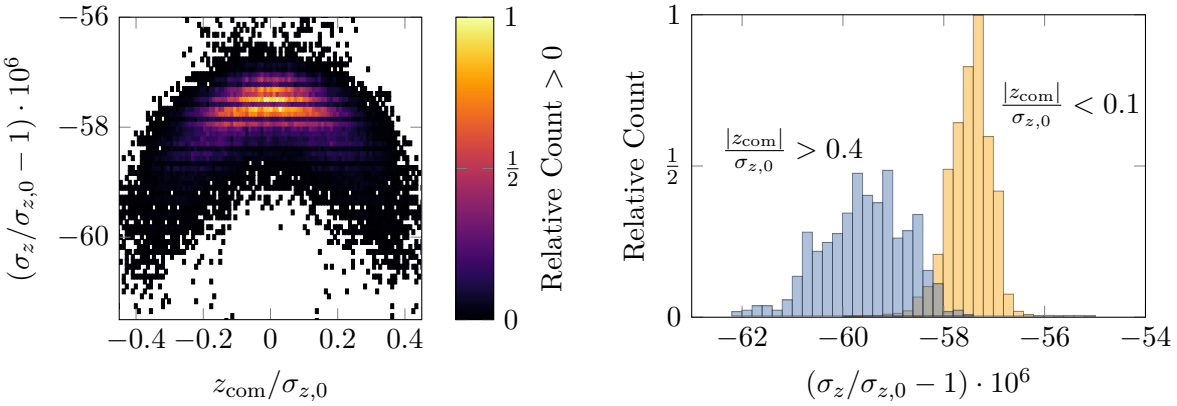

Figure 4.5.: Cyclic bunch lengthening due to coherent synchrotron oscillation in a *Inovesa* simulation (described in C.1). **(a)** Density histogram of the bunch lengths and bunch positions. **(b)** Bunch lengths for bunches categorised as central and extremal. Both plots demonstrate the correlation between bunch length and $|z_{\mathrm{com}}|$, which leads to a CSR modulation. Here, $\sigma_{z,0} \approx 6.8\,\mathrm{ps}$ and the relative bunch lengthening is of magnitude order 10^{-7}.

4.1.3. Multiplicative Noise

For completeness, the theoretical value of the mean square response in the presence of a multiplicative instability is given by [19]:

$$\left\langle \phi^2 \right\rangle' = \left\langle \phi^2 \right\rangle \left(\frac{1}{1 - \pi^2 \frac{f s^2 \tau_d}{f_0} \frac{\sigma_{\hat{V}}^2}{\hat{V}^2}} \right). \tag{4.5}$$

Although multiplicative noise by construction cannot excite an oscillation, it has an influence on the magnitude of coherent synchrotron oscillations. In the discrete model of the RF noise, it likewise does not appear due to the approximation (3.16b). Therefore equation (4.5) should only be applied in leading order of $\sigma_{\hat{V}}$.

In general, additive noise is the predominant mechanism governing the amplitude of the coherent synchrotron oscillation.

4.2. Effect on CSR

4.2.1. Phase Noise

To study the influence of phase noise in isolation, a RF instability of 2 mrad ($\approx 0.1\,^\circ$) has been added to the simulation. This keeps the root mean square (RMS) bunch position well below the bunch length. In normalised units,

$$\sigma_q = \sqrt{\langle q^2 \rangle} = \frac{\sqrt{\langle \phi^2 \rangle}}{2\pi h f_0 \sigma_{z,0}} \approx 0.3\,. \tag{4.6}$$

At this value there is adequate space for the bunch position to oscillate without a high probability for a significant density contribution outside the simulation domain of $q = [-6, 6]$. The RMS response in the oscillation phase was found to be $\sqrt{\langle \phi^2 \rangle} \approx 4.3\,\mathrm{mrad}$.

Due to the energy excursion of the bunch centre the Fokker-Planck contribution is generally non-zero independent of the bunch shape. This effect is illustrated in Fig. 4.5. The

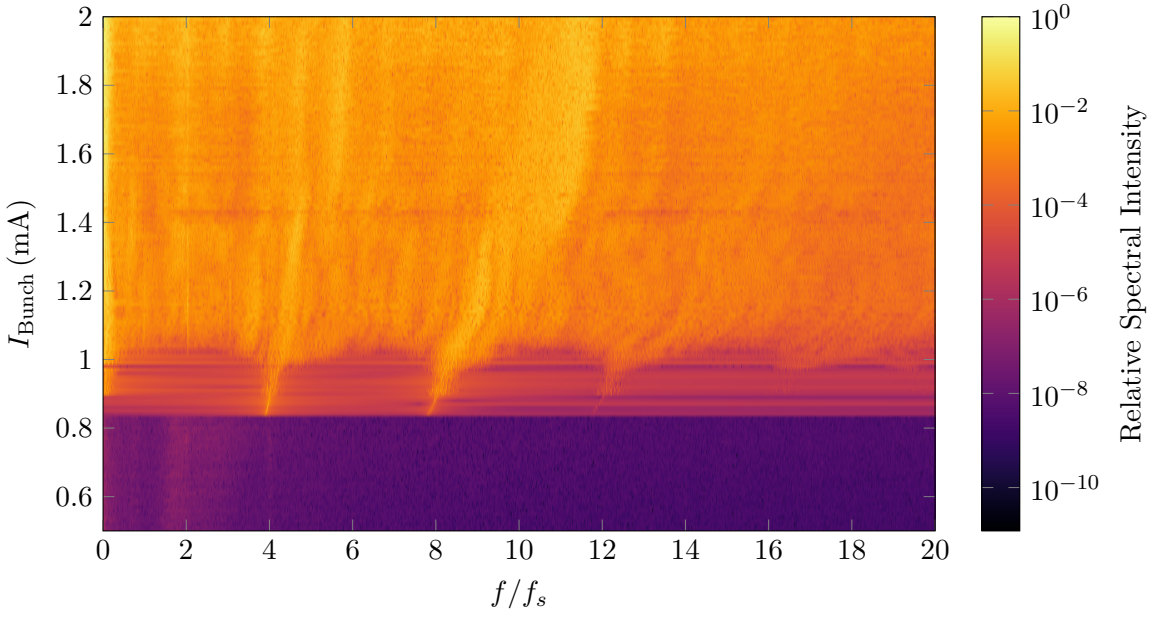

Figure 4.6.: Simulated bursting spectrogram of CSR sampled at $f_{\text{sample}} = 40\, f_s$. Parameters are listed in Appendix C.2. The weakly visible vertical spectral line at multiples of $2\, f_s$ is an artefact of charge renormalisation occurring at this frequency. Images created in Mathematica [18].

secondary CSR-yield associated with damping of a coherent oscillation is therefore largest near the antipodal longitudinal turning points, where the bunch is least spread out, and is modulated with $2f_s$. Although the CSR power modulation is small, it is highly regular and results in a bright spectral line in the bursting spectrogram.

The effect on the bursting spectrogram can be appreciated by comparing the response spectrogram 4.7 to the reference spectrogram 4.6 generated without noise.

Here, this line is emerging below the sawtooth threshold and dominating the former Haïssinski domain behaviour below. This domain is also uniformly amplified, resulting in a decreased dynamic range of the bursting spectrogram. Another spectral line is also present at $1f_s$, although less visibly. Given the flat spectral properties of the noise, a weak $1f_s$ modulation is expected, as is the periodic weak harmonic duplication.

There is experimental evidence for a CSR modulation at $2f_s$ related to coherent synchrotron oscillations of short bunches [5].

4.2.2. Amplitude Noise

The effect of an isolated amplitude instability of $\sigma_{\hat{V}}/\hat{V} = 1\%$ has been simulated, its bursting spectrogram is 4.8.

Even in the absence of intensity dependent effects, the consequence of a multiplicative instability is that the bunch shape is no longer subjected to a proper rotation. With that, the approximate rotational symmetry of the phase space distribution is lost. Analogue to the secondary effect of phase noise, the anisotropic phase space distribution causes a $2f_s$ modulation of the CSR signal. Low frequency modulations of the bunch shape on the time scale of a synchrotron period cause a regular modulation of the bunch shape. This irregularity is observed as an increase in the line width of the $2f_s$ modulation. In this simulation, the modulation of the CSR power is visible below the sawtooth bursting threshold, where a broad $2f_s$ modulation is observed.

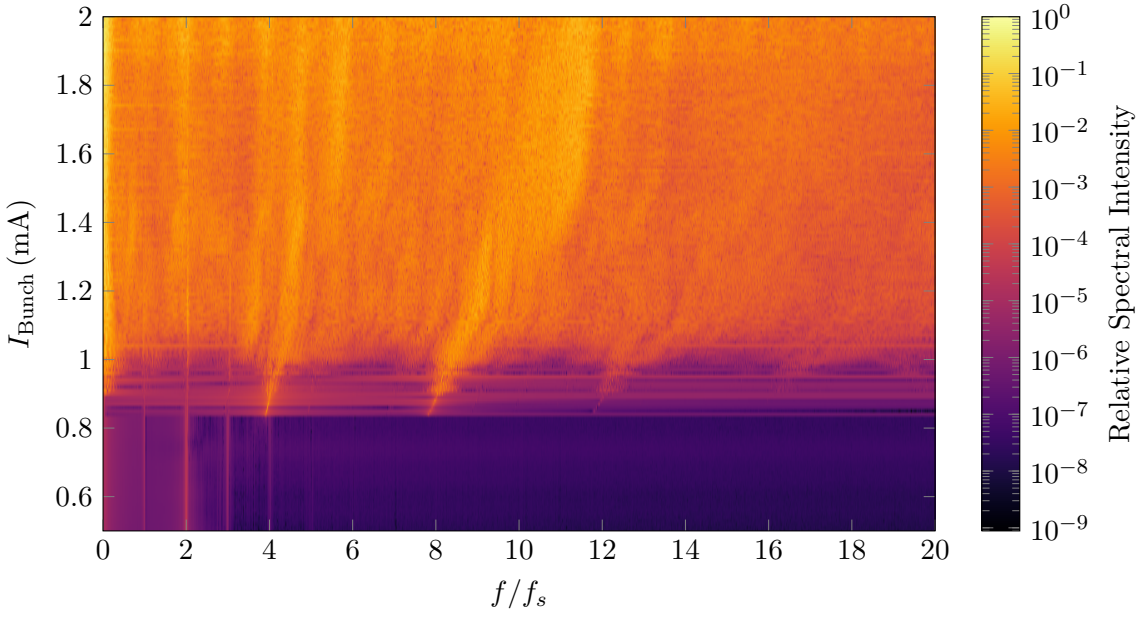

Figure 4.7.: Bursting spectrogram with a simulated phase noise $\sigma_{\phi s} = 2\,\mathrm{mrad}$. The $2f_s$ modulation due to a coherent synchrotron oscillation is clearly visible. The influence of noise on the bursting threshold is not resolved.

High frequency noise contributions cause a fast oscillation of the bunch length. Above the bursting threshold current, this effect is masked by the natural oscillations of the bunch length. Below the threshold such broad band CSR modulations are visible as horizontal lines varying in intensity.

4.2.3. Generic Noise

Another simulation with $\sigma_{\phi s} = 2\,\mathrm{mrad}$, $\sigma_{\hat{V}}/\hat{V} = 1\%$ has been evaluated (Fig. 4.9). The difference to the spectrogram 4.8 is negligible, since the effect of phase instability in the simulated quantity is perfectly masked by the amplitude instability. However, a reduction in the dynamic range of the power spectral intensity coefficients is observed. The introduction of physical noise therefore reduces the disparity between simulated and observed noise floor.

There is a small, consistent effect on the bursting threshold. Slightly above the regular bursting threshold at $I_{\mathrm{bunch}} = 835\,\mu\mathrm{A}$, the introduction of noise was found to inhibit microbunching. Evidence is given in Fig. 4.10. This may indicate that the effective intensity of a bunch undergoing length oscillations is reduced compared to a bunch with a reduced bunch length variance.

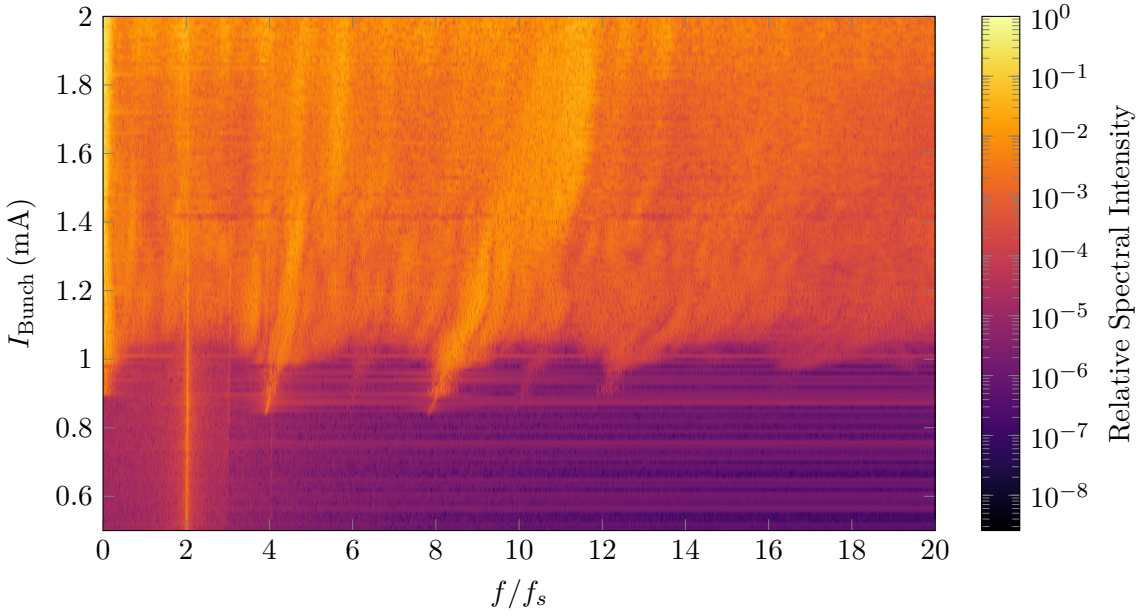

Figure 4.8.: Bursting spectrogram with a simulated amplitude noise $\sigma_{\hat{V}}/\hat{V} = 0.01$. The effect of a stochastic frequency in the rotation half-step is a periodic modulation of the bunch length with $2f_s$. Compared to the modulations due to coherent synchrotron oscillations caused by phase noise, the modulation is broader. Fourier analysis shows that the total modulation in the regular bursting regime has a spectral component near $6f_s$. This is observed in the spectrogram.

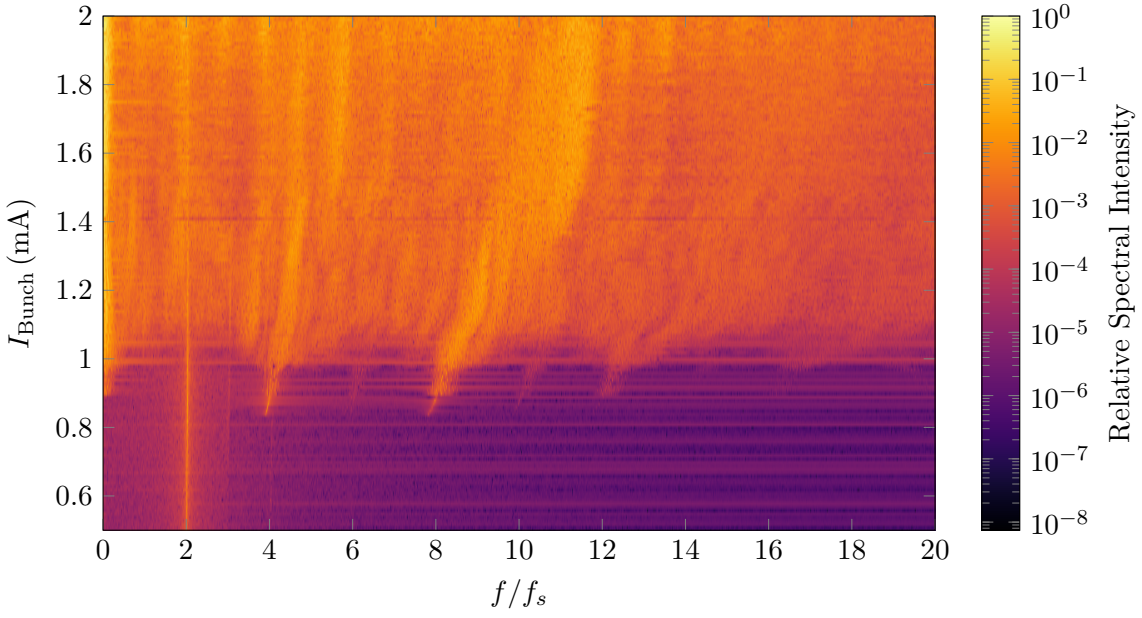

Figure 4.9.: Bursting spectrogram with a simulated phase noise $\sigma_{\phi s} = 2\,\text{mrad}$ and amplitude noise $\sigma_{\hat{V}}/\hat{V} = 0.01$. In these quantities, the effect of amplitude noise masks the effect of phase noise almost perfectly.

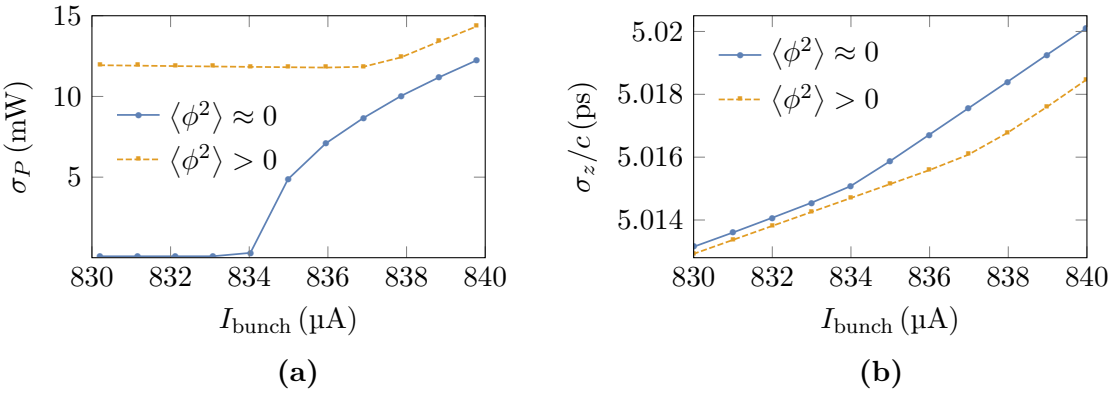

Figure 4.10.: Both the CSR power standard deviation **(a)** and the slope of the bunch length **(b)** signal the microbunching instability. Physical RF noise shifts the threshold in *Inovesa* (dashed). The CSR power modulation is included for a narrow band around $f = 4\,f_s$ to reduce the influence of modulations unrelated to the microbunching instability. Simulation parameters are listed in C.3.

5. Summary and Outlook

This thesis presents numerical studies of a physical RF noise in the longitudinal dynamics of a relativistic electron beam. Provided that the phase noise is sufficiently small, *Inovesa* results are self-consistent and qualitatively in agreement with experimental data. In conclusion, the implemented procedure allows the user to reliably reproduce coherent synchrotron oscillations in *Inovesa*.

The reproduction of the response to inevitable physical noise in a electron accelerator broadens the applicability of *Inovesa* results. As a side effect, physical noise masks numerical noise by raising the noise floor. This is especially relevant if simulation results are analysed next to measured data. The threshold for the microbunching instability is not found to change by an appreciable amount and coherent synchrotron oscillation does not account for the difference observed between simulation and measurement.

An instability in the momentum compaction can be applied analogous to RF noise to simulate the non-reproducible behaviour of bending and focusing magnets across turns. This leads to a potentially large multiplicative instability in the drift that may.

There are noise shapes beyond the studied Gaussian noise to investigate. For example, f_s-coloured additive noise leads to a response in $\langle\phi\rangle$, whereas the effect of multiplicative noise accumulates on the bunch shape in phase space. This may provoke a CSR response on a larger scale.

Appendix

A. Spectral Density of Discrete Gaussian White Noise

The energy instability amplitude $\sigma_{\delta\mathcal{E}}$ is equal to the scaled energy instability $\sigma'_{\delta\mathcal{E}}$ (3.11),

$$\sigma_{\delta\mathcal{E}} = \frac{1}{\sqrt{f_0\delta t}}\sigma'_{\delta\mathcal{E}}\,. \tag{A.1}$$

With (3.14) for $\delta\mathcal{E}'$,

$$e\hat{V}\sigma_{\phi s} = \frac{1}{\sqrt{f_0\delta t}}\left(f_0\delta t\, e\hat{V}\sigma'_{\phi s}\right). \tag{A.2}$$

The single cavity phase instability amplitude $\sigma_{\phi s}$ translates into the scaled instability amplitude $\sigma'_{\phi s}$ as

$$R(0) = \sigma'^2_{\phi s} = \frac{\sigma^2_{\phi s}}{f_0\delta t}\,. \tag{A.3}$$

The autocorrelation is given by the triangle function [12],

$$R(\tau) = \frac{\sigma^2_{\phi s}}{f_0\delta t}\max\left\{0, 1-\frac{|\tau|}{\delta t}\right\}. \tag{A.4}$$

The Wiener-Khinchin theorem relates autocorrelation and spectral density by Fourier transform [13]. The spectral density of the noise function using the above autocorrelation is given by

$$S(\omega) = \frac{1}{2\pi}\int_{-\infty}^{\infty} R(\tau)e^{-i\omega t}\mathrm{d}\tau \tag{A.5}$$

$$= \frac{\sigma^2_{\phi s}}{2\pi f_0\delta t}\int_{-\delta t}^{\delta t}\left(1-\frac{|\tau|}{\delta t}\right)e^{-i\omega\tau}\mathrm{d}\tau \tag{A.6}$$

$$= \frac{\sigma^2_{\phi s}}{2\pi f_0}\frac{2(1-\cos\omega\delta t)}{\omega^2\delta t^2}\,. \tag{A.7}$$

At the resonance $\omega = \omega_s$, the spectral density can be approximated by a constant corresponding to the equivalent white noise spectral density,

$$S(\omega)|_{\omega\delta t\ll\frac{\pi}{2}} \approx \lim_{\omega\to 0} S(\omega) = \frac{\sigma^2_{\phi s}}{2\pi f_0}\,. \tag{A.8}$$

B. Influence of the Rotation Angle and Grid Size

The choice of a time granularity inevitably distorts the result of the simulation outside of a stable interval. Here, the resiliency of the simulation with respect to the temporal density of simulation frames is evaluated. Therefore, the mean square response $\langle \phi^2 \rangle$ has been evaluated similar to C.1 at 341 exponentially spaced values between 403 and 2208 for the number of steps per synchrotron period N. Random numbers used as noise are uncorrelated across runs. By weighted linear regression, the fitted mean square response is given by

$$\left\langle \phi^2 \right\rangle (N) = 6.70 \cdot 10^{-6} + 1.34 \cdot 10^{-10} \cdot N \,. \tag{B.1}$$

This result is in agreement with the assumption of a response independent of N, and a large correlation in these variables is unlikely. On the other hand, there is empirical evidence for a functional relation between the *Inovesa* grid size and oscillatory response (Fig. B.1 (b)). The relative error is well below 1% across a wide range of grid sizes for the default *Inovesa* interpolation scheme.

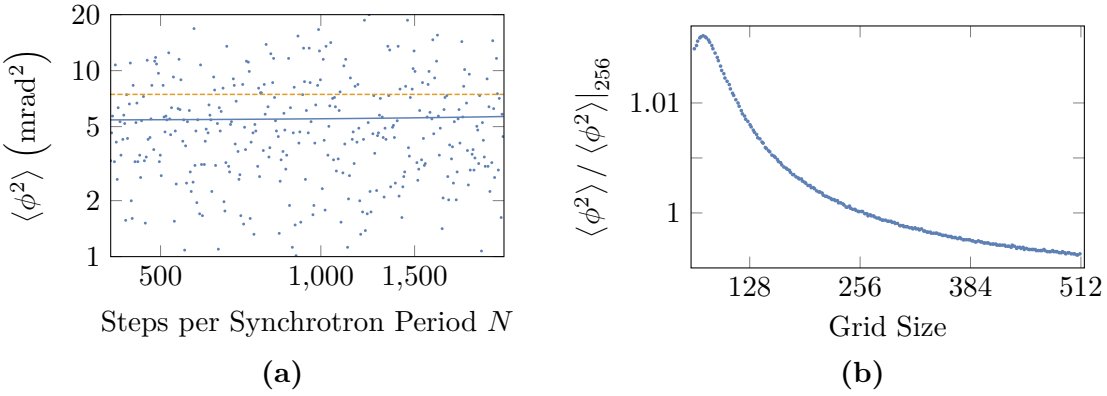

Figure B.1.: (a) Mean square response for simulations using different N. Displayed are the linear fit function (solid) and (4.2) (dashed). **(b)** The mean square response has a resonant functional dependence on the grid size, here displayed as a relative change compared to the result obtained at the default grid size of 256.

C. Simulation parameter table

C.1. Investigation of $\langle \phi^2 \rangle$

version	v0.14.RC10
I (mA)	3
Initial distribution	Zero centered Gaussian
Artificial Parameters	
f_{sample}	$10\, f_s$
$f_{\text{renormalisation}}$	$10\, f_s$
t	$100\, T_s$ and $10000\, T_s$
Physical Parameters	
τ_d	1 ms
f_0	9 MHz
f_s	45 kHz
$Z_{\parallel}$	0
h	50

C.2. Current Scan Spectrogram

Purpose	Reference	Phase Noise	Amplitude Noise	Generic Noise
Fig.	4.6	4.7	4.8	4.9
Version	v0.14.RC1	v0.14.RC10	v0.14.0	v1.0
I (mA)	$\{2, 1.99, \ldots, 0.5\}$			
Initial distribution	Zero centered Gaussian/adiabatic with $t_{\text{transition}} = 1000\, T_s$			
Artificial Parameters				
f_{sample}	$40\, f_s$			
$f_{\text{renormalisation}}$	$2\, f_s$	$10\, f_s$		
t	$250\, T_s$			
Physical Parameters				
τ_d	5 ms			
f_0	9 MHz			
f_s	30 kHz			
G	3.2 cm			
h	50			
$\sigma_{\phi s}$	0	2 mrad	0	2 mrad
$\sigma_{\hat{V}}/\hat{V}$	0	0	0.01	0.01

C.3. Threshold Region

	Reference	Generic Noise
version	v0.14.RC1	v0.14.RC10
I (mA)	$\{0.840, 0.839, .., 0.830\}$	
Initial distribution	Zero centered Gaussian/adiabatic with $t_{\text{transition}} = 1000\,T_s$	
Artificial Parameters		
f_{sample}	$40\,f_s$	
$f_{\text{renormalisation}}$	$10\,f_s$	
t	$250\,T_s$	
Physical Parameters		
τ_d	5 ms	
f_0	9 MHz	
f_s	30 kHz	
G	3.2 cm	
h	50	
$\sigma_{\phi s}$	0	5 mrad
$\sigma_{\hat{V}}/\hat{V}$	0	0.01

Bibliography

[1] H. Wiedemann, *Particle Accelerator Physics*. Graduate Texts in Physics, Springer, 4th ed., 2015.

[2] K.-Y. Ng, *Physics of Intensity Dependent Beam Instabilities*. Hackensack, NJ [u.a.]: World Scientific, 2006.

[3] G. L. Carr, S. L. Kramer, J. B. Murphy, J. LaVeigne, R. P. S. M. Lobo, D. H. Reitze, and D. B. Tanner, "Investigation of coherent emission from the NSLS VUV ring," in *Proceedings, 1999 Particle Accelerator Conference (PAC'99): New York, New York, March 29-April 2, 1999*, pp. 134–136, 1999.

[4] J. Byrd, W. Leemans, A. Loftsdottir, B. Marcelis, M. Martin, W. Mckinney, F. Sannibale, T. Scarvie, and C. Steier, "Observation of Broadband Self-Amplified Spontaneous Coherent Terahertz Synchrotron Radiation in a Storage Ring," *Physical review letters*, vol. 89, p. 224801, 12 2002.

[5] V. Judin, N. Hiller, A. Hofmann, E. Huttel, B. Kehrer, M. Klein, S. Marsching, C. Meuter, A.-S. Müuller, M. Nasse, M. Schuh, M. Smale, and M. Streichert, "Spectral and Temporal Observations of CSR at Anka," in *Proceedings, IPAC 2012 - International Particle Accelerator Conference 2012*, pp. 1623–1625, 2012.

[6] R. L. Warnock and J. A. Ellison, "A General Method for Propagation of the Phase Space Distribution, with Application to the Sawtooth Instability," in *The physics of high brightness beams. Proceedings, 2nd ICFA Advanced Accelerator Workshop, Los Angeles, USA, November 9-12, 1999*, pp. 322–348, 2000.

[7] P. Schönfeldt, M. Brosi, M. Schwarz, J. L. Steinmann, and A.-S. Müller, "Parallelized Vlasov-Fokker-Planck solver for desktop personal computers," *Phys. Rev. Accel. Beams*, vol. 20, p. 030704, Mar 2017.

[8] H. Wiedemann, *Synchrotron Radiation*. Berlin: Springer, 2003.

[9] K. Wille, *Physik der Teilchenbeschleuniger und Synchrotronstrahlungsquellen*. Stuttgart: Teubner, 1996.

[10] E. J. Jaeschke *et al.*, *Synchrotron Light Sources and Free-Electron Lasers: Accelerator Physics, Instrumentation and Science Applications*. Cham: Springer, 1st ed. 2016 ed., 2016.

[11] S. Y. Lee, *Accelerator Physics*. Hackensack, N.J: World Scientific, 2. ed ed., 2007.

[12] P. E. Kloeden and E. Platen, *Numerical Solution of Stochastic Differential Equations*. Berlin: Springer, 1992.

[13] K. W. Ormond and J. T. Rogers, "Synchrotron Oscillation Driven by RF Phase Noise," in *Proceedings, 17th IEEE Particle Accelerator Conference (PAC 97)*, vol. C970512, p. 1822, 1997.

[14] J. B. Murphy, S. Krinsky, and R. L. Gluckstern, "Longitudinal Wake Field for an Electron Moving on a Circular Orbit," *Part. Accel.*, vol. 57, pp. 9–64, 1997.

[15] M. Brosi *et al.*, "Fast Mapping of Terahertz Bursting Thresholds and Characteristics at Synchrotron Light Sources," *Phys. Rev. Accel. Beams*, vol. 19, no. 11, p. 110701, 2016.

[16] N. Hiller, A. Borysenko, E. Hertle, E. Huttel, V. Judin, B. Kehrer, S. Marsching, A. S. Müller, M. J. Nasse, A. Plech, M. Schuh, N. J. Smale, B. Steffen, P. Peier, and V. Schlott, "Electro-optical Bunch Length Measurements at the ANKA Storage Ring," in *IPAC 2013: Proceedings of the 4th International Particle Accelerator Conference*, pp. 500–502, 2013.

[17] L. Rota *et al.*, "KALYPSO: A Mfps Linear Array Detector for Visible to NIR Radiation," in *Proceedings, 5th International Beam Instrumentation Conference (IBIC 2016): Barcelona, Spain, September 11-15, 2016*, p. WEPG46, 2017.

[18] W. R. Inc., "Mathematica, Version 11.2." Champaign, IL, 2017.

[19] K. Lindenberg, V. Seshadri, K. E. Shuler, and B. J. West, "Equal-Time Second-Order Moments of a Harmonic Oscillator with Stochastic Frequency and Driving Force," *Journal of Statistical Physics*, vol. 23, pp. 755–765, Dec 1980.